Journal of CO2 Utilization 82 (2024) 102765

Contents lists available at ScienceDirect

Journal of CO2 Utilization

journal homepage: www.elsevier.com/locate/jcou

Solar photothermo-catalytic conversion of CO_2 on phyllosilicates modified with Ni and CeO_2

Giusy Dativo [a], Eleonora La Greca [a,b], Leonarda Francesca Liotta [b], Valeria La Parola [b], Marcello Condorelli [a], Giuliana Impellizzeri [c], Giuseppe Compagnini [a], Salvatore Sciré [a,d], Roberto Fiorenza [a,c,d,*]

[a] Department of Chemical Sciences, University of Catania, V.le A. Doria 6, Catania 95125, Italy
[b] Institute for the Study of Nanostructured Materials (ISMN), National Research Council (CNR), Via Ugo La Malfa 153, Palermo 90146, Italy
[c] Institute for Microelectronics and Microsystems (IMM), National Research Council (CNR), Via S. Sofia 64, Catania 95123, Italy
[d] C.I.R.C.C. (Interuniversity Consortium in Chemical Reactivity and Catalysis) UdR of Catania, V.le A. Doria 6, Catania 95125, Italy

ARTICLE INFO

Keywords:
Carbon dioxide
Integrated CO_2 conversion
Phyllosilicate
Ni
CeO_2

ABSTRACT

One of the strategies to mitigate the greenhouse effect is converting the CO_2 into high-added value products. In this work, a photothermo-catalytic approach, using peculiar Ni-phyllosilicates samples, was applied for the CO_2 conversion into solar fuels. In particular, the Ni-phyllosilicates were modified with the introduction of the Ce ions in their structure and successively they were covered with the CeO_2 semiconductor. The structural, morphological, textural, optical and reducibility properties as well as the interaction with CO_2 were investigated. The Ni/Ce-phyllosilicate covered with CeO_2 achieved a CO_2 conversion of 87% after 5 hours of photothermo-catalytic test using simulated solar irradiation at 120°C, producing 15.8 $\mu mol/g_{cat}\bullet h$ of CO and 5.6 $\mu mol/g_{cat}\bullet h$ of CH_4. The same sample was tested in an integrated approach where the CO_2 was evolved by the catalytic oxidation of toluene and then was converted into CO and CH_4, obtaining a CO_2 conversion of 50% and 8.8 $\mu mol_{CO}/g_{cat}\bullet h$ and 3.3 $\mu mol_{CH4}/g_{cat}\bullet h$. The presence of Ni in the phyllosilicates structure guaranteed a good catalytic stability whereas the deposition of CeO_2 allowed to exploit the improved thermal (redox) properties of cerium oxide and favoured the CO_2 adsorption on its basic sites and oxygen vacancies. Furthermore, the high surface area of the as-synthetized Ni-phyllosilicates permitted to efficiently expose the CeO_2 surface-active sites to the solar radiation. The here investigated catalysts showed versatile properties ideal for hybrid catalytic approaches as the photothermo-catalysis, allowing to propose new solutions for the CO_2 valorization.

1. Introduction

Nowadays, the increase of the greenhouse effect and the necessity to favour the decarbonization of the processes make the technologies of the CO_2 valorisation, as the Carbon Capture and Storage (CCS) and the Carbon Capture and Utilization (CCU), valuable and sustainable solutions for the mitigation of the carbon dioxide emission. CCU make also possible to obtain high-added value products from this gas [1]. In this context, the solar photocatalytic CO_2 conversion into solar fuels is one of the most fascinating process that mimics the natural photosynthesis, giving chemicals (CO, CH_4, CH_3OH, etc.), that could be used by the industries with a zero-carbon balance, thus increasing the overall sustainability [2].

Unfortunately CO_2 is a very stable molecule with strong bonds between carbon and oxygen, consequently, considerable energy is required for its conversion [3]. Therefore, the thermocatalytic CO_2 conversion is an energy-consuming process (it requires temperatures higher than 200°C) with a poor stability of the employed catalysts [4]. Conversely, the bare solar photocatalytic CO_2 reduction, using the most common semiconductors as the TiO_2-based materials, suffers of two main drawbacks as an inefficient solar light absorption and a high charge carriers recombination that strongly limits the yields into solar fuels [5].

Recently, a hybrid catalysis, as the photothermo-catalysis, has emerged as promising solution that favoured the CO_2 conversion into solar fuels working at lower temperatures compared to the thermocatalytic approach, and obtaining, at the same time, higher performance respect to both the solar photocatalysis and the thermocatalysis [6].

* Corresponding author at: Department of Chemical Sciences, University of Catania, V.le A. Doria 6, Catania 95125, Italy.
E-mail address: rfiorenza@unict.it (R. Fiorenza).

https://doi.org/10.1016/j.jcou.2024.102765
Received 9 February 2024; Received in revised form 7 April 2024; Accepted 10 April 2024

Moreover, the high versatility of this methodology allows to use catalysts able to absorb visible and infrared photons with a more efficient harvesting of the solar spectrum. In addition, with proper materials, it is possible to exploit the increase of the global/local temperature of the catalyst surface during the reaction, in order to overcome the equilibrium limit of the thermocatalytic reaction, further improving, in this way, the CO_2 conversion [7,8].

For this purpose, the proper catalysts should exhibit both photocatalytic and thermocatalytic (redox) features. In recent works, we demonstrated that the TiO_2-CeO_2 composites with the addition of small amounts of co-catalysts (CoO-CuO) can efficiently promote the photothermo-catalytic CO_2 conversion into CO and CH_4 at relative low temperature (120°C), with higher performance compared to the corresponding photocatalytic and thermocatalytic approaches [9]. The performance was enhanced, especially in terms of CH_4 formation, if the TiO_2 was properly supported on porous materials as some basic zeolites, that favoured the adsorption of CO_2 on their sites, whereas the CO_2 conversion was boosted up by the photothermo-catalytic properties of cuprous oxide added as co-catalyst [10].

However, since 2020 the Ti metal entered in the EU critical raw material list, and this was also confirmed in the 2023 updated list [11]. Therefore, the choice of proper catalysts is a key parameter to propose new and sustainable alternatives to the most employed materials [12].

On the basis of these considerations, in this work the performance of peculiar phyllosilicates (ps) modified with Ni and Ce ions and coated with CeO_2 (ceria) were examined. The phyllosilicates are green materials widely used in catalysis [13–15] and recently also in photocatalysis [16]. Their structure consists of continuous tetrahedral and octahedral sheets [15] and their textural properties combined with the possibility to incorporate different ions make them an ideal support and/or catalyst for different applications.

In particular, we have synthetized Ni-ps considering the good catalytic properties of Ni, that is widely used in the reforming reactions at high temperatures, and for its very strong interaction with silica that led to an excellent stability and carbon resistance [15,17]. Furthermore, Ni-based catalysts are widely used in CO_2 reduction reactions thanks to peculiar features of this metal resembling those of more expensive noble metals [18,19]. Likewise, Ni-based materials are employed also in photocatalysis due to their interesting optical properties, as the significant visible light absorption in the UV–vis region and the surface plasmon resonance effect [20,21].

The addition of Ce ions into the ps structure and the following coating with cerium oxide allowed to exploit the redox properties of the Ce ions and to further promote the CO_2 adsorption on the ceria basic sites [9]. Besides, CeO_2 is a semiconductor that showed both photocatalytic and photothermo-catalytic properties [9,22]. Recently, *Cheng et al.* [23] have demonstrated as it is possible to favour selectively the photocatalytic reduction of CO_2 to CH_4, by anchoring single atomic Co on the S-scheme heterojunctions made by CeO_2/carbon nitride, highlighting the possibility of strongly increasing the performance of CeO_2 by opportune chemical and/or structural modifications.

The performance of the best examined ps-based catalyst was also tested in an integrated approach where the CO_2 was evolved by the thermocatalytic oxidation of toluene (a model volatile organic compound, VOC) in gas-phase and subsequently, this CO_2 was converted into solar fuels. Indeed, recently the integrated CO_2 capture and/or conversion (ICC) gained considerable attention due to the direct possibility to obtain high-added value products from pollutants or from waste through the conversion of the formed CO_2 [24,25].

2. Materials and methods

2.1. Catalyst preparation

$Ni(NO_3)_2{\cdot}6H_2O$, $Mg(NO_3)_2{\cdot}6H_2O$, $Ce(NO_3)_3{\cdot}6H_2O$, NaOH, $Na_2SiO_3{\cdot}5H_2O$, $Cu(NO_3){\bullet}5/2H_2O$, KOH were used as-purchased from Merck.

2.1.1. Preparation of phyllosilicates with Ni and Ce ions: Ni/Ce-ps

A modified hydrothermal method was used for the synthesis of the ps [26]. Specifically, 1.4 g of cerium nitrate hexahydrate and 0.6 g of nickel nitrate hexahydrate were added to 24 mL of deionized water and solubilized. Successively 1.3 g of sodium metasilicate pentahydrate was added to 11 mL of deionized water, adding this latter solution to the previous one. The obtained solution was stirred for 30 minutes at room temperature. After, 3.2 g of NaOH was added to the solution and stirred for other 20 minutes. Afterwards, the solution was transferred to an autoclave, heated at 160°C for 48 hours. The obtained precipitate was centrifuged and washed twice with water and ethanol (50:50). The powders were therefore filtered, dried for 12 hours at 60°C and calcinated at 600°C for 2 hours. This catalyst was coded as Ni/Ce-ps.

2.1.2. Preparation of phyllosilicates with Ni and Ce coated with CeO_2: Ni/Ce-ps@CeO_2

The coating of CeO_2 on the as-prepared Ni/Ce-ps was made by chemical precipitation [27]. In particular, 500 mg of Ni/Ce-ps (uncalcined) and 825 mg of cerium nitrate hexahydrate were added to 100 mL of water. The solution was stirred at 70°C for 3 hours, adding dropwise a solution of KOH 1 M until pH=9 was reached. The solution was left to decant overnight and then was filtered. The solid catalyst was dried at 60 °C for 12 hours and calcined at 600 °C for 2 hours. This catalyst was named Ni/Ce-ps@CeO_2. The bare CeO_2 used for the catalytic comparison was synthetized with the same chemical precipitation approach, following the procedures reported in the ref. [27].

2.1.3. Preparation of phyllosilicates with Ni and Ce coated with CuO: Ni/Ce-ps@CuO

Another modified Ni phyllosicate sample was prepared replacing the coating of CeO_2 with the CuO. The synthesis was the same reported above substituting the cerium nitrate hexahydrate with copper nitrate hemipentahydrate and adopting the same thermal treatments. This catalyst was coded as Ni/Ce-ps@CuO.

2.1.4. Preparation of phyllosilicate with Ni: Ni-ps

For comparison, the Ni-ps was prepared using the same procedures of the Ni/Ce-ps substituting the cerium nitrate hexahydrate with the magnesium nitrate hexahydrate.

2.2. Samples characterization

The Raman spectroscopy was performed using the second harmonic (532 nm) of an Nd:YAG laser in the backscattering mode with a Witec Alpha 300 RS instrument. For all the examined materials, the power of the exciting laser was 5 mW and the acquisition time and accumulation number were fixed respectively at 10 seconds and 10 spectra.

Powder X-ray diffraction (XRD) patterns were recorded on a Bruker D5005 diffractometer equipped with a Cu-Kα radiation ($\lambda = 1.5418$ Å) and a graphite monochromator on the diffracted beam. The XRD data were generally collected in the 2θ range of 10°–80° with a scanning step size of 0.02° and 0.5 s.

The FTIR spectra were performed with a Spectrum Two System (Perkin Elmer), using KBr powders as reference.

The SEM images were obtained with a ZEISS SUPRA 55 VP equipped with an energy dispersive X-ray (EDX) INCA-Oxford windowless detector.

The textural properties of the powders were measured by Brunauer-Emmett-Teller (BET) with the physisorption of N_2 at −196 °C using a Micromeritics Tristar II Plus 3020, pre-treating the samples at 150 °C overnight.

The UV–vis DRS (Diffuse Reflectance Spectroscopy) spectra were acquired with a JASCO V-670. The optical band-gap of the samples (E_g) was evaluated graphing the modified Kubelka–Munk function vs the hν

[28]. It is important to note that the application of this method to composite materials can lead to an inaccurate estimation of the band-gap values. Indeed, as reported [28,29], the reflectance spectra of these samples are more complex compared to bare semiconductor oxides with homogenous crystalline phase. Therefore, it is not easy to discriminate the transition modes and to extrapolate the E_g values.

The CO_2-TPD (Temperature Programmed Desorption) measurements were performed in a fixed bed quartz reactor filled with 150 mg of sample. After the adsorption and the surface saturation process, the CO_2 flow (30 cc/min) was stopped. Afterwards the reactor was heated from 30°C to 600°C (rate of 5 °C/min). The CO_2 desorption peaks were recorded with a mass spectrometer (Sensorlab VG Quadrupoles). Before the measurements the powders were pre-treated with a He flow (30 cc/min) for 1 h at 150°C.

Hydrogen Temperature Programmed Reduction (H_2-TPR) measurements were carried out with the Automated Catalyst Characterization System AutoChem 2950HP (Micromeritics) equipped with a thermal conductivity detector (TCD). About 0.120 g of a sample was used for each measurement. The samples were pre-treated with a mixture of 5 vol % O_2 in He at 50 cc/min, heated up (10 °C/min) to 400 °C, and held at this temperature for 30 min. After cooling down to room temperature, the gas mixture of 5 vol% H_2 in Ar was introduced at 30 cc/min into the sample tube and was also used as a reference gas. During the analysis, the temperature was increased up to 1000 °C with a rate of 10 °C/min. The effluent gas was analysed with the TCD.

The X-ray photoelectron spectroscopy (XPS) analyses were carried out with a VG Microtech ESCA 3000 Multilab (VG Scientific, Sussex, UK), equipped with a dual Mg/Al anode. Unmonochromatized Al K radiation was used as an excitation source (1486.6 eV). All the binding energies were referred to the C 1 s energy, previously calibrated at 285.1 eV, arising from adventitious carbon. Qualitative and quantitative analyses of the peaks were performed using CasaXPS software (version 2.3.17, Casa Software Ltd. Wilmslow, Cheshire, UK, 2009). A precision of ± 0.15 eV on the binding energy values and of ± 10%. on the atomic percentages was considered.

2.3. Photothermo-catalytic conversion of CO_2

The catalytic tests were performed with a cylindrical batch Pyrex reactor, filled with 0.2 g of catalyst, irradiating for 5 h with a solar lamp (Osram Ultra Vitalux 300 W, irradiance of 10.7 mW/cm^2) and heating with an isomantle heater settled at 120°C. A mixture of CO_2 and H_2O vapour was flowed in the photoreactor to achieve the saturation of the catalyst surface with the reagent molecules. The water vapour produced from a bubbler was mixed with CO_2 (99.999%) [9]. With a mass flow controller, the CO_2/H_2O mixture was regulated in order to have a molar ratio of 15, necessary to favour the CO_2 reduction rather than the competitive water splitting reaction [30].

The reaction products were examined with the Agilent 6890 N gas chromatograph (HP-PLOT Q column, TCD detector) calibrated for the detection of methane and carbon monoxide, and with the Trace GC instrument (Porapak Q column, FID detector) used to detect the possible formation of other organic compounds. Before the tests the samples were reduced in a hydrogen atmosphere (10 cc/min) for 2 h at 600°C and the samples surface pre-cleaned from possible carbonaceous residues following the procedures reported in the supporting information. The CO_2 conversion values were determined with the following equation:

$$CO_2\text{conversion}: \left(\frac{\text{Area}_{\text{peak CO2in}} - \text{Area}_{\text{peak CO2out}} \times \left(\frac{\text{Area}_{\text{peak standard in}}}{\text{Area}_{\text{peak standard out}}} \right)}{\text{Area}_{\text{peakCO2in}}} \right) \times 100$$

Furthermore, also the mass balance method was applied, considering the following equation:

$$CO_2\text{conversion}: \left(\frac{\text{Area}_{\text{peak CO2out}}}{\text{Area}_{\text{peak products out}} + \text{Area}_{\text{peak CO2out}}} \right) \times 100$$

The two methods were in accordance each other (±5%, reproducibility 95%).

2.4. Photothermo-catalytic integrated CO_2 conversion (ICC)

The used experimental set-up for the ICC tests is illustrated in the supporting information (Fig. S1). In particular, the catalytic oxidation of toluene was carried out in a heated flow reactor. The reaction was performed continuously at atmospheric pressure using 150 mg of 5%wt MnO_x-5%wt CuO_x/TiO_2 sample chosen as the best catalyst, in our experimental conditions, to favour the total oxidation of toluene into CO_2 [31]. The details of the preparation of this catalyst are reported in the supporting information. The reactor was heated with a programmable oven with a heating ramp of 5 °C/min from 30°C to 370°C, temperature at which the total combustion of toluene was verified (Figs. S2). Before the tests, the reactant mixture (0.4 vol% VOCs; 10 vol % air, rest He) was adsorbed–desorbed over the catalyst for 30 min to assure the steady-state. With this procedure, conversion and selectivity were within 3–5% of reproducibility. Preliminary runs performed at different flow rates demonstrated the absence of external diffusional limitations. The absence of internal diffusional limitations was instead assured by running experiments with different grain size powders. We excluded the occurrence of heat transfer limitations because we found that the temperature of the reactor at different heights was substantively the same, reasonably due to the low concentration of the reactants used in the catalytic tests. The flow rate of the reactant mixture was 60 cc/min. The effluent gases were examined on-line by a gas chromatograph, equipped with a packed column with 10% FFAP on ChromosorbW and FID detector, and by a quadrupole mass spectrometer (VG quadrupoles). The carbon balance was always higher than 95%. The evolved CO_2 was flowed in the cylindrical Pyrex batch photoreactor described in the paragraph 2.3 adopting the same experimental procedures.

3. Results and discussion

3.1. Photothermo-catalytic conversion of CO_2 into solar fuels: screening of the synthesized phyllosilicates

In the Fig. 1 are reported the data obtained from the photothermo-catalytic conversion of CO_2 into CO and CH_4 (the only products obtained in our experimental conditions) using pure CO_2. It is clear that the addition of Ce ions in the structure of Ni-ps strongly improved the photothermo-catalytic activity with the CO_2 conversion that increased from 4% of Ni-ps to 77% of Ni/Ce-ps. A further improvement was verified with the coating of CeO_2, indeed the Ni/Ce-ps@CeO_2 sample reached the 87% of CO_2 conversion, enhancing of 16 times the production of CO and CH_4 compared to the bare Ni-ps. As reported, the presence of cerium oxide allowed to exploit its photocatalytic and photothermo-catalytic properties, also favouring the CO_2 adsorption on its basic sites [9,25,32,33]. Furthermore, the presence of Ce ions in the structure of the ps can additionally promote the adsorption of carbon dioxide due to the possible formation of oxygen vacancies, preferential sites where the CO_2 was adsorbed [34,35].

In accordance with the literature, on the CeO_2-based (photo)catalysts CO was the most common solar fuel formed from the CO_2 conversion in the gas-phase [9,32]. Indeed, although the evolution of methane is thermodynamically favoured ($CO_2 + 8\,H^+ + 8e^- \rightarrow CH_4 + 2\,H_2O$ $E^0 = -0.24$ V at pH=7) compared to the formation of CO ($CO_2 + 2\,H^+ + 2e^- \rightarrow CO + H_2O$ $E^0 = -0.53$ V at pH=7), kinetically the CH_4 formation is more difficult than that of CO, requiring the synchronous reaction among the CO_2, 8 photoelectrons and 8 protons whereas CO evolution involves only

2 electrons and 2 protons [32].

It is important to highlight that to efficiently activate the photothermo-catalytic features of cerium oxide it was necessary its deposition on Ni/Ce-ps. In fact, the photothermo-catalytic activity of the bare CeO_2 was much lower respect to the Ni/Ce-ps@CeO_2 sample (Fig. 1). The peculiar structure of the ps allowed to better expose the CeO_2 surface-active sites to the simulated solar irradiation and to the heating [10], whereas the presence of the Ni and the Ce ions in the structure of ps efficiently activated the CO_2 allowing to increase the overall performance of the catalyst.

Conversely, the coating with CuO was less efficient compared to the Ni/Ce-ps@CeO_2, reasonably due both to the tendence of CuO to favour photocorrosion phenomena and to its rapid charge carriers recombination [10,36]. For these reasons the Ni/Ce-ps@CeO_2 was chosen as best sample to investigate the photothermo-catalytic methodology and for the ICC test.

On the basis of the definitions of *Ma et al.* [6] the photothermo-catalytic approach here used can be better identified in a photo-assisted thermocatalysis (activity of photocatalysis near to zero, activity of the combined approach higher than the bare thermocatalysis) or in a photo-driven thermocatalysis (activity of photocatalysis near to zero, activity of the combined approach with self-heating effects due to the properties of the catalysts, greater or equal than the thermocatalysis). In our experimental conditions the activity of the Ni/Ce-ps@CeO_2 in the bare solar photocatalytic tests at room temperature was very low (Table 1). The heating was necessary to activate the CO_2 and to promote the desorption of the solar fuels. However, it was possible to exclude photo-driven thermocatalytic effects, whose conditions required an increase of the local temperature of the catalyst surface to favour the reaction, because the surface temperature of the Ni/Ce-ps@CeO_2 measured by an infrared thermo-camera remained substantially the same before and after the photothermo-catalytic CO_2 conversion at 120°C (Fig. S3). This points to as the combined action of the heating and the simulated solar light was fundamental to increase the CO_2 conversion through a photo-assisted thermocatalytic mechanism that allowed to use milder conditions (120°C) with respect to the bare thermocatalytic tests. Indeed, with the same catalyst no activity was detected in the bare thermocatalytic tests (in the dark) at temperatures lower than 300°C, whereas the activity in the bare solar photocatalysis (without heating) was much lower compared to the photo-assisted thermocatalytic measurements (Table 1).

Finally, it is possible to note a decrease in the activity of the catalyst in the solar photo-assisted thermocatalysis increasing the reaction temperature, this is probably associated with the sintering of the Ni and/or of the CeO_2 particles [9,17,22].

3.2. Integrated CO_2 conversion obtained from the catalytic oxidation of toluene: ICC test

The photothermo-catalytic activity of the Ni/Ce-ps@CeO_2 catalyst was also tested in an integrated test where the CO_2 was produced by the catalytic oxidation of toluene (see the experimental section and the supporting information for the details).

In this case, the Ni/Ce-ps@CeO_2 exhibited lower activity both in terms of μmol/g_{cat}h of products and CO_2 conversion (%) compared to the results of the test with pure CO_2 (see Figs. 1 and 2). Reasonably, the CO_2 coming from the catalytic oxidation of toluene contains, also in traces, not-converted toluene or other byproducts gases which can substantially affect the catalytic activity [25]. Moreover, Fig. 2 shows that the activity of the Ni/Ce-ps@CeO_2 catalyst decreases over time (10% of the CO_2 conversion was lost along 40 hours of time-on stream). It is known that the reduction in H_2 flow of the Ni-ps-based samples was a key pre-treatment step to activate them in the CO_2 reduction reaction [37]. Reasonably, during the continuous and simultaneous irradiation and heating, the Ni tend to sinter [38,39] and to re-oxidise (as verified by XPS commented in the Section 3.4), leading to a decrease of the interaction between the CeO_2 and the Ni/Ce-ps. However, the obtained results seem promising being similar of those obtained with TiO_2-CeO_2 based samples (using the same experimental set-up, with a CO_2 conversion of 52% after 5 h of integrated CO_2 conversion test) [25].

Table 1
Comparison of the different catalytic approaches using the Ni/Ce-ps@CeO_2 sample in the CO_2 reduction.

	CO_2 conversion (%)	CO formation (μmol/g_{cat}•h)	CH_4 formation (μmol/g_{cat}•h)
Solar photo-assisted thermocatalysis*	86.9 (120°C)	15.8 (120°C)	5.6 (120°C)
	74.3 (220°C)	13.5 (220°C)	4.8 (220°C)
	67.6 (320°C)	12.3 (320°C)	3.5 (320°C)
Thermocatalysis	no activity (120°C)	/ (120°C)	/ (120°C)
		/ (220°C)	/ (220°C)
	no activity (220°C)	2.8 (320°C)	1.0 (320°C)
	15.6 (320°C)		
Solar photocatalysis*	5.2 (r. T.)	0.9 (r.T.)	0.3 (r.T.)

* After 5 h of simulated solar irradiation

3.3. Samples characterizations: structural, textural, morphological and optical properties

The structural properties of Ni-ps, Ni/Ce-ps and Ni/Ce-ps@CeO_2 were investigated by Raman spectroscopy (Fig. 3). The presence of CeO_2 (fluorite type phase) was confirmed by the main Raman band at around 463 cm^{-1} present in the Ni/Ce-ps and Ni/Ce-ps@CeO_2 samples [40]. This latter phyllosilicate, due to the coating with cerium oxide, showed another band at 561 cm^{-1} related to the presence of oxygen vacancies [41]. At these species, formed due to the presence of Ce^{3+} ions, are assigned also the bands at 226 and 632 cm^{-1} also showed in the Ni/Ce-ps sample [42]. Furthermore, the Ni/Ce-ps catalyst exhibited a band at 968 cm^{-1} probably due to the second-order longitudinal optical mode of ceria [43]. Finally, the broad bands centred at 866, 1005, 1055, and 1076 cm^{-1} were typical of phyllosilicates, arising from the symmetric stretching vibration of Si–O_{nb} bonds (O_{nb}= non-bridging oxygen with another Si) in the $(Si_xO_y)^z$ units [44]. In the Ni-ps sample another broad band centred at around 522 cm^{-1}, visible also in the Ni/Ce-ps sample, can be attributed, considering the adopted synthesis [26], to Na-rich montmorillonite-based structures [44,45]. No bands were directly related to the Ni, this is an indication of the incorporation of the metal in the structure of the phyllosilicates [46].

Similar conclusions can be drawn by the XRD spectra (Fig. S4). In the Ni/Ce-ps and Ni/Ce-ps@CeO_2 patterns are clear the diffraction peaks related to CeO_2 at 2Θ = 28.4°,33.1°, 47.5°, 56.1°, 76.7° and 79.1°,

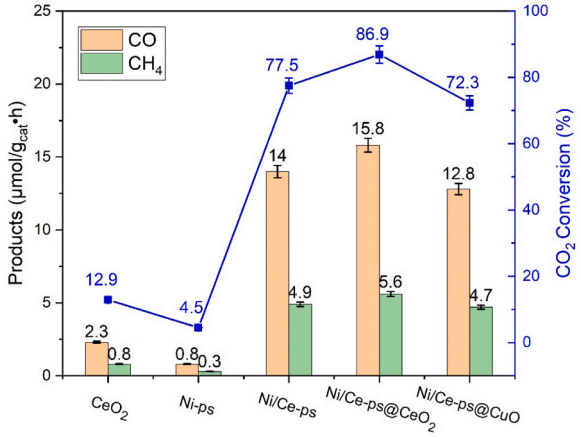

Fig. 1. Photothermo-catalytic CO_2 reduction at T = 120 °C after 5 h of simulated solar irradiation.

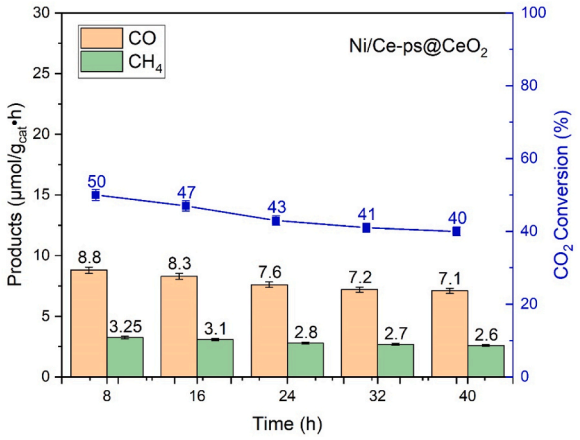

Fig. 2. Photothermo-catalytic CO_2 reduction at T = 120 °C in the integrated CO_2 conversion tests with the Ni/Ce-ps@CeO_2 sample.

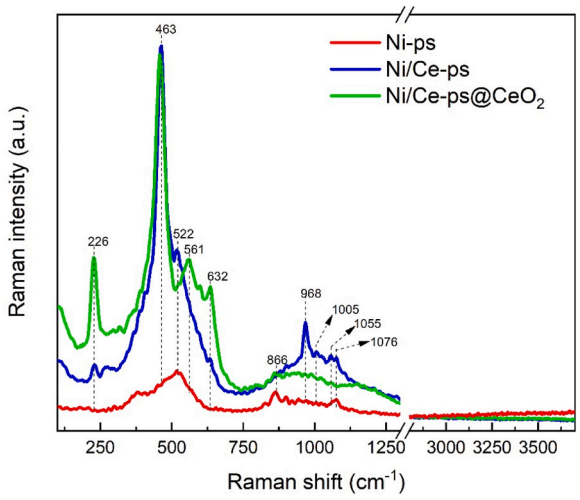

Fig. 3. Raman spectra of the examined phyllosilicates.

accordingly to the ICSD reference. In the Ni/Ce-ps@CeO_2 another peak at about 2Θ = 31.4° can be assigned to the Ni-based phyllosilicates structure [47], whereas the small feature at about 2Θ = 43.4° can be associated to the presence of Ni (as NiO). The XRD pattern of Ni/ps showed many diffraction peaks reasonably related to the presence of Na-based silicates and Na-rich montmorillonite-based structures [48], in accordance with the Raman spectra. Probably, the addition of Ce ions and the successive covering of CeO_2 allowed to remove the excess of Na from the structure of the ps, with the CeO_2 formed both inside the bulk than on the surface of ps [26]. Indeed, from the SEM-EDX analysis (Figs. S5, Table S1) of the Ni/Ce-ps@CeO_2 sample was not detected the presence of Na (EDX analysis of the other samples Figs. S6-S7, Table S2-S3). Furthermore, the sample showed the typical morphology of the montmorillonite-based phyllosilicates (Fig. S5) [49]. Finally, the presence of the phyllosilicates structure was further verified by FT-IR (Fig. S8). All the samples showed a broad band centred at about 922 cm^{-1} associated to the Si-O-Si bonds, whereas the broad bands at lower wavenumbers (< 600 cm^{-1}) were related to the metal-oxygen-metal vibrational modes (metal=Ce, Ni [50]). The Ni-ps showed another band at around 1451 cm^{-1} reasonably assigned to O-C-O stretching vibration due the formation of Na-based carbonates generated from the excess of Na that interacted with the atmospheric carbon dioxide [51].

No substantial variation was observed in the optical band gap measurements (Table 2) estimated by the UV–vis DRS spectra (Fig. S9A) and the modified Kubelka-Munk function (Fig. S9B). The incorporation of the Ce ions and the following coating with cerium oxide allowed only to slightly decrease the optical band gap value of Ni-ps, with the Ni/Ce-ps@CeO_2 sample that showed a wider feature in the visible region compared to the other samples, associated to the covering of CeO_2 (Fig. S9A) [52,53].

Table 2
Optical and textural properties of the examined phyllosilicates samples.

Samples	Optical band gap (eV)	BET surface area (m^2/g)	Mean pore diameter (nm)	Pore volume (cm^3/g)
Ni-ps	3.3	38	25.1 1.	0.28
Ni/Ce-ps	3.0	51	8.5	0.20
Ni/Ce-ps@CeO_2	3.0	101	4.2	0.15

The textural properties of the examined ps-based samples are reported in the Table 2 and in Fig. 4. In accordance with Raman and XRD analysis there were significant differences among the three phyllosilicates. In particular, the Ni-ps showed the lowest BET surface area with a type III isotherm and a H3 hysteresis loop, usually associated to aggregate or plate-like particles with slit-shaped pores [54]. The same sample exhibited the largest mean pore diameter and pore volume (Table 2, Fig. 4B). Probably, the agglomeration of the particles was favoured in this catalyst due to excess of sodium and the presence of several Na-based silicates structures (as detected by XRD and Raman). Conversely, the introduction of Ce ions allowed to increase of 13 m^2/g

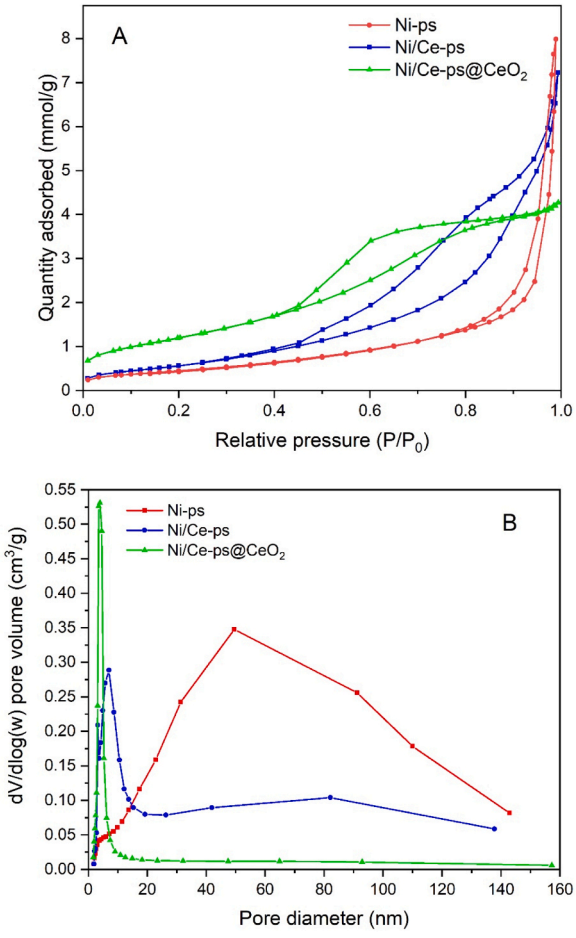

Fig. 4. N_2 physisorption curves (A) and Barrett-Joyner-Halenda (BJH) pore size distribution (B, desorption curve) of the examined samples.

the surface area with a narrower pore size distribution. The Ni/Ce-ps showed indeed a larger H3 hysteresis loop. The coating of CeO_2 radically changed the textural properties of the ps-based samples. The Ni/Ce-ps@CeO_2 own the highest surface area (101 m^2/g) and a type IV isotherm with a H2 hysteresis that it is related to pores with wide bodies and narrow necks [54]. The highest value of surface area, the lowest dimension of pores and the better exploitation of the visible light portion of the solar spectrum can be other key factors to explain the highest photothermo-catalytic activity of the Ni/Ce-ps@CeO_2 sample in the CO_2 reduction reaction.

3.4. Discussion

The modification of Ni-phyllosilicates samples with the inclusion of Ce ions and the coating with CeO_2 allowed to obtain an efficient photothermo-catalyst for the CO_2 conversion into solar fuels, both in a single approach (use of pure CO_2) than in an integrated mode, where the carbon dioxide was evolved by the catalytic combustion of a dangerous volatile organic compound. The introduction of Ce ions in the Ni-ps structure permitted indeed, to increase the surface area (Table 2) and to favour the adsorption of CO_2, due to the formation of oxygen vacancies, as detected by Raman. The further coating with the CeO_2 semiconductor promoted the photothermo-catalytic activity thanks to both the redox (thermoactivated) and the photocatalytic properties of ceria [9,22]. Furthermore, the presence of additional basic sites related to the CeO_2 can facilitate the activation of CO_2, boosting up its conversion. A confirmation of this positive features of the CeO_2 coating was showed in the CO_2-TPD curves reported in the Fig. 5.

The profiles can be divided in three zones denoted as α, β and γ, and concerned to weak, medium and strong basic sites, respectively [55]. For the CO_2 conversion neither too weak nor too strong basic sites favoured the reaction. Indeed, the weakly CO_2 adsorbed cannot be activated, as well as the too strong CO_2 adsorbed makes the activated CO_2 difficult to transfer and consequently to convert [56,57].

From the Fig. 5 it is clear as the coating with CeO_2 of the Ni/Ce-ps@CeO_2 sample allowed to have a wide CO_2 desorption peak centred at 122°C between the α and the β zones that can be considered a good compromise to have basic sites able to promote the activation and the subsequent conversion of CO_2. Moreover, the temperature of this wide CO_2-TPD peak is equal to the temperature used for the photothermo-catalytic test (120°C), whereby during the reaction with the Ni/Ce-ps@CeO_2 catalyst the CO_2 was rapidly activated and converted, favouring the formation of the solar fuels.

All the ps-based catalysts showed a desorption peak at 40°C attributed to the interaction between the surface -OH groups of the ps and the CO_2 [58]. The Ni-ps sample also exhibited another peak at 69°C and a wide feature between the β and the γ zone. Reasonably, in this sample too weak and too strong basic sites did not favour the CO_2 conversion and this explains the lowest activity of this sample (Fig. 1). The introduction of Ce ions in the Ni/Ce-ps sample facilitated the CO_2 adsorption due to the presence of the oxygen vacancies formed by the introduction of these ions into the ps structure (as confirmed by Raman). The oxygen vacancies in fact, were preferential sites for the CO_2 adsorption [34,35]. Consequently, the CO_2-TPD profile of the Ni/Ce-ps sample showed several peaks in the region between the α and the β zones. The deposition of CeO_2 in the Ni/Ce-ps@CeO_2 catalyst led the formation of moderate basic sites that improves the photothermo-catalytic CO_2 conversion.

The beneficial effects of the heating in the photo-assisted thermo-catalytic CO_2 conversion and in the ICC test allowed to activate also the redox properties of CeO_2. In this contest the H_2-temperature-programmed reduction (TPR) profiles of the examined samples (Fig. 6) highlight the reducibility features of the Ni/Ce-ps@CeO_2 sample.

The TPR profile of Ni-ps sample exhibited a notable peak centered at 680°C, that was ascribed to the reduction of Ni^{2+} to Ni^0 [34,47]. In the Ni/Ce-ps, a comparable peak was detected at lower temperature (669°C), whereas in the Ni/Ce-ps@CeO_2 sample, a well-defined shoulder emerged at 620°C [59]. These temperature shifts towards lower values suggested that the reducibility of Ni has been promoted to the incorporation of Ce ions into the phyllosilicate structure. However, the profile of Ni/Ce-ps catalyst is distinctly different from the Ni-ps catalyst and includes contribution from the partial reduction of ceria as well. In fact, the broad peak at 605°C was associated with the reduction of Ce^{4+} to Ce^{3+}, a process typically occurring in the range of 550°-700°C [60]. Moreover, it was reported in literature that the Ni^{2+} ions that are incorporated into the CeO_2 lattice during catalyst preparation induced lattice deformation, inequality the charge balance of CeO_2 and generating oxygen vacancies [61]. Consequently, oxygen species adsorbed on these vacancies became readily reducible at lower temperatures. Furthermore, the Ni/Ce-ps@CeO_2 sample displayed a wide peak centered at 509°C and a low-temperature reduction peak at 339°C. These peaks were associated with the reduction of surface-defective CeO_2 and the reduction of oxygen species adsorbed on the oxygen vacancies of ceria [60,62]. Therefore, in this sample the CeO_2 showed improved redox properties, activated at lower temperatures compared to the conventional CeO_2-based catalysts [60].

In Table 3 the experimental H_2 consumption values for Ni-ps, Ni/Ce-ps and Ni/Ce-ps@CeO_2 catalysts are listed and compared with the theoretical uptakes calculated assuming complete reduction of Ni^{2+} to Ni^0 and full reduction of Ce^{4+} to Ce^{3+}. As regards the Ni-ps sample, the experimental and theoretical values well agree showing that more than 90% of Ni^{2+} was reduced to the metallic state. On the other hand, it can

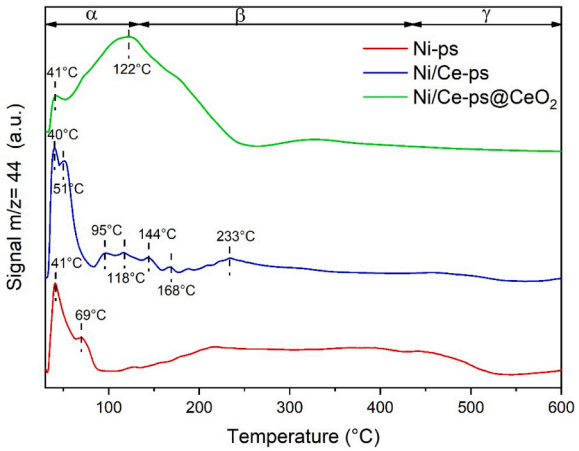

Fig. 5. CO_2-TPD profiles of the ps-based samples.

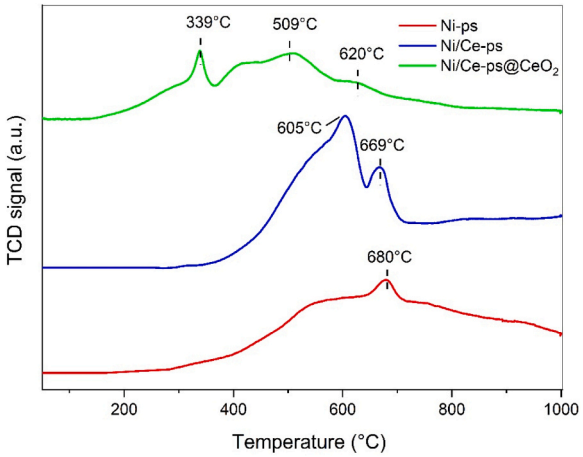

Fig. 6. H_2-TPR profiles of the ps-based samples.

Table 3
Experimental hydrogen consumption values and theoretical data.

Catalyst	Experimental H_2 consumption (mL/g_{cat})	Theoretical consumption for Ni^{2+}/Ni^0 reduction (mL/g_{cat})	Theoretical consumption for Ce^{4+}/Ce^{3+}reduction (mL/g_{cat})
Ni-ps	52.8	58.4	-
Ni/Ce-ps	79.7	66.7	36.7
Ni/Ce-ps@CeO_2	43.2	18.5	63.2

be assumed that some Ni oxidized strongly interacting with the support is difficult to be reduced.

Notably, the TPR profiles for Ni/Ce-ps and Ni/Ce-ps@CeO_2 encompass the contribution from the partial reduction of CeO_2. By comparing the values listed in Table 3, it is difficult to evaluate the extent of ceria reduction occurring in the present samples. Indeed, ceria reduction strongly depends on preparation steps and as well on the crystallinity and defective structure of the oxide [60–62]. Accordingly, the experimental H_2 consumption values of the two catalysts, Ni/Ce-ps and Ni/Ce-ps@CeO_2, strongly differ and we can not evaluate the extent of reduction of the oxidized species. By comparison with the theoretical consumption requested for Ni^{2+} reduction it can be argued that metallic Ni is formed in all the reduced samples, while the remaining hydrogen consumption can be attributed to the reduction of ceria differently distributed on the catalyst. On the other hand, the absence of the typical reduction profile of ceria oxide characterized by a surface and bulk reduction peaks, at around 400 and 800 °C, respectively [60–62] further confirms the presence of defective ceria oxide in both Ce-containing catalysts.

In summary, the synthesis of the Ni-ps modified with the addition of the Ce ions and the following covering with CeO_2, allowed to improve the photothermo-catalytic performance of both the Ni-ps and the cerium oxide obtaining at the end a versatile catalyst with interesting properties and a good activity in the conversion of CO_2 into solar fuels. In particular, the presence of CeO_2 and of its oxygen vacancies led to enhance the adsorption/activation of CO_2, that was converted into CO and CH_4 with a photo-assisted thermocatalytic mechanism. The possible reaction scheme with the best sample (Ni/Ce-ps@CeO_2 sample) is illustrated in the Fig. 7. In this multicatalytic approach the temperature allowed to facilitate the CO_2 activation, the desorption of the formed solar fuels and the activation of the redox properties of CeO_2. Contextually, the CeO_2 distributed on the surface of the Ni/Ce-ps efficiently exposed its surface-active sites to the solar photons allowing the formation of electrons (e^-) and holes (h^+) in the conduction band (CB) and in the valence band (VB), respectively [63,64]. The holes were able to oxidize the water vapor, added both in the photothermo-catalytic CO_2 conversion reaction and in the ICC test, to produce the protons necessary for the reduction of CO_2. The heating facilitated the mobility of these protons that should react synchronously with the e^- and the adsorbed CO_2 [9,10,25,65]. The presence of the oxygen vacancies, due to the introduction of Ce ions in the ps structure, the high surface area and the basic sites of CeO_2 favoured the adsorption of the CO_2 molecules with a moderate strength (as detected by CO_2-TPD). All these features were ideal to favour the reaction with the e^- and H^+ to generate the solar fuels.

To get insight into the surface interaction of Ni and Ce in the Ni/Ce-ps@CeO_2 sample and the specific role of Ni towards the stability of the sample, the XPS characterization was carried out before and after the integrated approach test (Fig. 8)

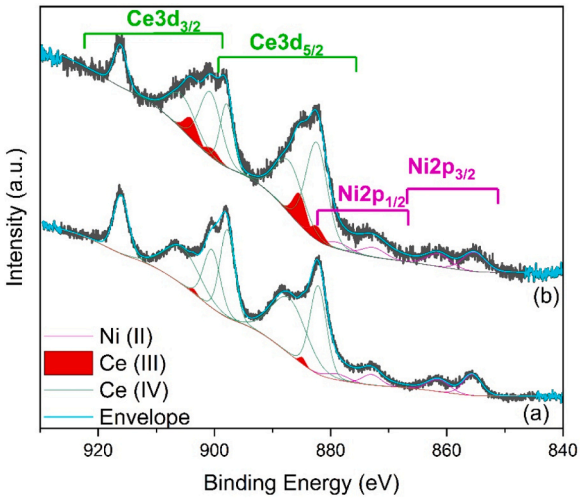

Fig. 8. Ce3d and Ni2p region for the Ni-Ce-ps@CeO_2 catalyst (a) before and (b) after the photothermo-catalytic CO_2 conversion at T = 120 °C in the integrated approach (40 h of time-on stream test).

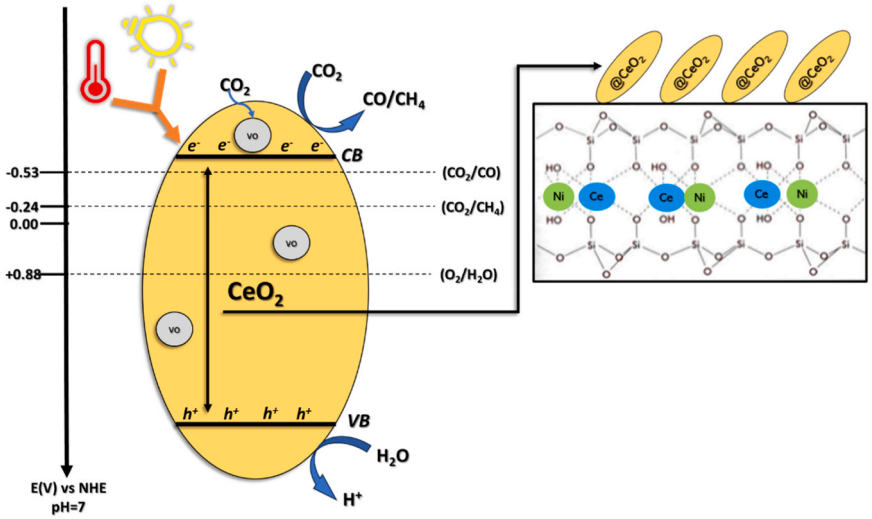

Fig. 7. Proposed photothermo-catalytic mechanism with the Ni/Ce-ps@CeO_2 catalyst. Vo represents an oxygen vacancy.

The binding energy region, displayed in the Fig. 8, is quite intricate due to the composite nature of these peaks. Ni2p shows the presence of the spin splitting coupling which gives rise to $Ni2p_{3/2}$ and $Ni2p_{1/2}$, each of these peaks with a shake-up satellite. Ce3d is split in 10 components arising from different Ce4f level occupancies in the final state [66]. Six of these components are attributed to Ce(IV) and four to Ce(III). Moreover, there is an overlapping of the $Ni2p_{1/2}$ peaks and $Ce3d_{5/2}$. The fitting of the Ce3d peak has been done according to the treatment suggested by Burrogh [66–68] and commonly accepted. The fresh sample contains mainly Ce (IV) with a small presence of Ce (III) (*ca.* 2% of the total amount of cerium). After catalytic reaction the amount of Ce (III) increases notably reaching 14%. Nickel oxidation state does not change during reaction. The profile is typical of Ni(II) with a shake-up at ca. 6 eV. The position of the $Ni2p_{3/2}$ at 855.2 eV, higher than the value of pure NiO, indicates a metal support interaction between Ni and Ce [69, 70] as also verified by H_2-TPR. This interaction does not change due to catalytic reaction. The relative ratio of Nickel over Cerium measured by XPS is 0.28 in the fresh sample and slightly increases to 0.31 in the spent sample suggesting a surface migration of nickel during reaction (further details about the XPS analysis and the information about the other samples are reported in the supporting information).

Therefore, the presence of Ni in the ps structure guaranteed the catalytic stability, allowing to maintain the CO_2 conversion value between 50% and 40% (Fig. 2) during the integrated CO_2 conversion test even after prolonged and simultaneous processes of heating and irradiation. Furthermore, the good interaction between Ni and Ce, promoted by the ps structure, allowed to efficiently activate the photocatalytic and the thermocatalytic (redox) properties of CeO_2, boosting up the CO_2 conversion into solar fuels.

The good performance of the Ni/Ce-ps@CeO_2 catalyst and the possibility to use the phyllosilicates as green material to support semiconductor photocatalysts led to consider this peculiar material a promising alternative to the conventional catalysts and photocatalysts. Moreover, the possibility to incorporate several ions into the ps structure allowed to efficiently design performing catalysts. In particular, in this work it was highlighted as the addition of Ce ions in the Ni-ps structure improved the CO_2 adsorption/activation thanks to the formation of oxygen vacancies. Moreover, the further covering of the as-prepared Ni/Ce-ps with CeO_2 allowed to modify and to amplify the photothermocatalytic properties of this semiconductor, leading to increase the catalytic performance. Therefore, the here reported synthesis can be also considered a sustainable and performing way to improve the performance of CeO_2 semiconductor, that, especially in photocatalysis, required structural and/or chemical modifications to show a remarkable activity [22,25].

Finally, the application of a hybrid catalytic approach as the photothermo-catalysis, to further enhance the production of the solar fuels, can increase the appealing of the CO_2 valorisation technologies.

4. Conclusions

The modification of Ni-phyllosilicates samples with the introduction of Ce ions and the subsequent covering with CeO_2, allowed to efficiently improve the photothermo-catalytic properties of both Ni-phyllosilicates and CeO_2. In particular, the synergisms activated by a photo-assisted thermocatalytic approach and between the phyllosilicates and the cerium oxide permitted to obtain the 87% and the 50% of the CO_2 conversion using pure carbon dioxide and the CO_2 evolved by the catalytic oxidation of toluene in an integrated approach, respectively. The basic sites and the oxygen vacancies of CeO_2 favoured the CO_2 adsorption and activation, the high surface area of the phyllosilicates allowed to efficiently expose the surface-active sites of CeO_2 to the simulated solar irradiation, whereas the heating further promoted the CO_2 activation and conversion. The application of the photothermo-catalysis for the CO_2 conversion is promising because permitted to use simple and green materials whose combination with semiconductor photocatalysts can be a straightforward way to promote the formation of solar fuels from the carbon dioxide.

CRediT authorship contribution statement

Salvatore Sciré: Writing – review & editing, Supervision, Resources. **Giuseppe Compagnini:** Supervision, Resources. **Roberto Fiorenza:** Writing – review & editing, Writing – original draft, Validation, Supervision, Investigation, Data curation, Conceptualization. **Valeria La Parola:** Writing – review & editing, Methodology, Investigation, Data curation. **Leonarda Francesca Liotta:** Writing – review & editing, Validation, Methodology, Investigation, Data curation. **Giuliana Impellizzeri:** Validation, Investigation. **Marcello Condorelli:** Investigation. **Eleonora La Greca:** Investigation, Data curation. **Giusy Dativo:** Writing – review & editing, Writing – original draft, Investigation, Data curation, Conceptualization.

Declaration of Competing Interest

The authors declare that they have no known competing financial interests or personal relationships that could have appeared to influence the work reported in this paper.

Data Availability

Data will be made available on request.

Acknowledgements

The authors thank the Bio-nanotech Research and Innovation Tower (BRIT) laboratory of the University of Catania for the Raman facility. R. Fiorenza thanks the European Union (NextGeneration EU) MUR-PRIN PNRR 2022 "CO2@photothermocat" project (CUP E53D23015700001) for the support. G. Dativo, and S. Scirè thank the Sicilian Micro and Nano Technology Research and Innovation Center (SAMOTHRACE, CUP E63C22000900006). G. Compagnini thanks the European Union (NextGeneration EU) MUR-PRIN PNRR 2022 "Enhanced LAser spectroscopy TEchniques for autism Diagnosis in children (ELATED)" project (CUP E53D23015780001). L.F. Liotta thanks the "NEST - Network 4 Energy Sustainable Transition" (PE00000021, PNRR, NextGeneration EU, D.D. MUR Prot. n. 1561 11/10/2022). E. La Greca thanks the University of Perugia for the national PhD scholarship in catalysis.

Appendix A. Supporting information

Supplementary data associated with this article can be found in the online version at doi:10.1016/j.jcou.2024.102765.

References

[1] Y. Jafri, J.M. Ahlström, E. Furusjö, S. Harvey, K. Pettersson, E. Svensson, E. Wetterlund, Double yields and negative emissions? Resource, climate and cost efficiencies in biofuels with carbon capture, storage and utilization, Front. Energy Res. 10 (2022) 797529, https://doi.org/10.3389/fenrg.2022.797529.

[2] M. Du, M. Xing, S. Kang, Y. Ma, B. Qiu, Y. Chai, Building a bridge from solid wastes to solar fuels and chemicals via artificial photosynthesis, EcoMat 4 (2022) e12259, https://doi.org/10.1002/eom2.12259.

[3] J. Schneider, H. Jia, J.T. Muckerman, E. Fujita, Thermodynamics and kinetics of CO_2, CO, and H^+ binding to the metal centre of CO_2 reduction catalysts, Chem. Soc. Rev. 41 (2012) 2036–2051, https://doi.org/10.1039/C1CS15278E.

[4] Y. Li, S.H. Chan, Q. Sun, Heterogeneous catalytic conversion of CO_2: a comprehensive theoretical review, Nanoscale 7 (2015) 8663–8683, https://doi.org/10.1039/C5NR00092K.

[5] L. Ran, J. Hou, S. Cao, Z. Li, Y. Zhang, Y. Wu, B. Zhang, P. Zhai, L. Sun, Defect engineering of photocatalysts for solar energy conversion, Sol. RRL 4 (2020) 1900487, https://doi.org/10.1002/solr.201900487.

[6] R. Ma, J. Sun, D.H. Li, J.J. Wei, Review of synergistic photo-thermo-catalysis: Mechanisms, materials and applications, Int. J. Hydrog. Energy 45 (2020) 30288–30324, https://doi.org/10.1016/j.ijhydene.2020.08.127.

[7] W. Gao, Y. Li, D. Xiao, D. Ma, Advances in photothermal conversion of carbon dioxide to solar fuels, J. Energy Chem. 83 (2023) 62–78, https://doi.org/10.1016/j.jechem.2023.04.024.

[8] S. Fang, Y.H. Hu, Thermo-photo catalysis: a whole greater than the sum of its parts, Chem. Soc. Rev. 51 (2022) 3609–3647, https://doi.org/10.1039/D1CS00782C.

[9] R. Fiorenza, M. Bellardita, S.A. Balsamo, L. Spitaleri, A. Gulino, M. Condorelli, L. D'Urso, S. Scirè, L. Palmisano, A solar photothermocatalytic approach for the CO_2 conversion: Investigation of different synergisms on CoO-CuO/brookite TiO_2-CeO_2 catalysts, Chem. Eng. J. 428 (2022) 131249, https://doi.org/10.1016/j.cej.2021.131249.

[10] R. Fiorenza, C. Contarino, V. Spanò, M.T.A. Iapichino, S.A. Balsamo, Photothermocatalytic strategies for the CO_2 valorisation using TiO_2-based composites, Catal. Today 423 (2023) 114251, https://doi.org/10.1016/j.cattod.2023.114251.

[11] M. Grohol, C. Veeh, Study on the Critical raw Materials for the E-Final report, European Commission, Brussels, 2023. doi/10.2873/725585.

[12] J. Wang, M. Zhang, Z. Chen, L. Li, G. Jiang, Z. Li, Enabling enhanced photocatalytic hydrogen evolution in water by doping Cs_2SnBr_6 perovskite with Pt, ACS Energy Lett. 9 (2024) 653–661, https://doi.org/10.1021/acsenergylett.4c00144.

[13] S. Nawaz, M. Ahmad, S. Asif, J.J. Klemeš, M. Mubashir, M. Munir, M. Zafar, A. Bokhari, A. Mukhtar, S. Saqib, K.S. Khoo, P.L. Show, Phyllosilicate derived catalysts for efficient conversion of lignocellulosic derived biomass to biodiesel: A review, Bioresour. Technol. 343 (2022) 126068, https://doi.org/10.1016/j.biortech.2021.126068.

[14] D.-T. To, Y.-C. Lin, Copper Phyllosilicates-derived catalysts in the production of alcohols from hydrogenation of carboxylates, carboxylic acids, carbonates, formyls, and CO_2: a review, Catalysts 11 (2021) 255, https://doi.org/10.3390/catal11020255.

[15] Z. Bian, S. Kawi, Preparation, characterization and catalytic application of phyllosilicate: a review, Catal. Today 339 (2020) 3–23, https://doi.org/10.1016/j.cattod.2018.12.030.

[16] C. Li, N. Zhu, S. Yang, X. He, S. Zheng, Z. Sun, D.D. Dionysiou, A review of clay based photocatalysts: role of phyllosilicate mineral in interfacial assembly, microstructure control and performance regulation, Chemosphere 273 (2021) 129723, https://doi.org/10.1016/j.chemosphere.2021.129723.

[17] Z. Bian, Z. Li, J. Ashok, S. Kawi, A highly active and stable Ni-Mg phyllosilicate nanotubular catalyst for ultrahigh temperature water-gas shift reaction, Chem. Commun. 51 (2015) 16324–16326, https://doi.org/10.1039/c5cc05226b.

[18] L. Baharudin, N. Rahmat, N.H. Othman, N. Shah, S.S.A. Syed-Hassan, Formation, control, and elimination of carbon on Ni-based catalyst during CO_2 and CH_4 conversion via dry reforming process: a review, J. CO_2 Util. 61 (2022) 102050, https://doi.org/10.1016/j.jcou.2022.102050.

[19] Y. He, Y. Zhou, J. Feng, M. Xing, Photothermal conversion of CO_2 to fuel with nickel-based catalysts: a review, Environ. Funct. Mater. 1 (2022) 204–217, https://doi.org/10.1016/j.efmat.2022.07.003.

[20] S. Kim, J. Kim, J. Park, J. Nam, Nonnoble-metal-based plasmonic nanomaterials: recent advances and future perspectives, Adv. Mater. 30 (2018) 1704528, https://doi.org/10.1002/adma.201704528.

[21] J. Li, Z. Lou, B. Li, Nanostructured materials with localized surface plasmon resonance for photocatalysis, Chin. Chem. Lett. 33 (2022) 1154–1168, https://doi.org/10.1016/j.cclet.2021.07.059.

[22] M. Bellardita, R. Fiorenza, L. D'Urso, L. Spitaleri, A. Gulino, G. Compagnini, S. Scirè, L. Palmisano, Exploring the photothermo-catalytic performance of Brookite TiO_2-CeO_2 composites, Catalysts 10 (2020) 765, https://doi.org/10.3390/catal10070765.

[23] L. Cheng, X. Yue, J. Fan, Q. Xiang, Site-specific electron-driving observations of CO_2-to-CH_4 photoreduction on Co-doped CeO_2 /crystalline carbon nitride S-scheme heterojunctions, Adv. Mater. 34 (2022) 2200929, https://doi.org/10.1002/adma.202200929.

[24] J. Chen, Y. Xu, P. Liao, H. Wang, H. Zhou, Recent progress in integrated CO_2 capture and conversion process using dual function materials: a state-of-the-art review, Carbon Capture Sci. Technol. 4 (2022) 100052, https://doi.org/10.1016/j.ccst.2022.100052.

[25] R. Fiorenza, M. Bellardita, S.A. Balsamo, A. Gulino, M. Condorelli, G. Compagnini, S. Scirè, L. Palmisano, A solar photothermo-catalytic combined process for the VOCs combustion and the subsequent CO_2 valorization using noble metal-free catalysts, Catal. Today (2023) 113949, https://doi.org/10.1016/j.cattod.2022.11.010.

[26] H. Shi, C. Tian, X. Liu, N. Sun, C. Song, H. Zheng, K. Gao, X. Wang, Z. Jiang, Y. Xuan, Y. Ding, Ni-phyllosilicate nanotubes coated by CeO_2 for ultra-efficiency of 36.9% and near-limit CO_2 conversion in solar-driven conversion of CO_2-to-fuel, Chem. Eng. J. 454 (2023) 140063, https://doi.org/10.1016/j.cej.2022.140063.

[27] R. Fiorenza, S.A. Balsamo, M. Condorelli, L. D'Urso, G. Compagnini, S. Scirè, Solar photocatalytic H_2 production over CeO_2-based catalysts: Influence of chemical and structural modifications, Catal. Today 380 (2021) 187–198, https://doi.org/10.1016/j.cattod.2021.02.003.

[28] P. Makuła, M. Pacia, W. Macyk, How to correctly determine the band gap energy of modified semiconductor photocatalysts based on UV–Vis spectra, J. Phys. Chem. Lett. 9 (2018) 6814–6817, https://doi.org/10.1021/acs.jpclett.8b02892.

[29] B. Ohtani, Photocatalysis A to Z—What we know and what we do not know in a scientific sense, J. Photochem. Photobiol. C. Photochem. Rev. 11 (2010) 157–178, https://doi.org/10.1016/j.jphotochemrev.2011.02.001.

[30] E. Karamian, S. Sharifnia, On the general mechanism of photocatalytic reduction of CO_2, J. CO_2 Util. 16 (2016) 194–203, https://doi.org/10.1016/j.jcou.2016.07.004.

[31] R. Fiorenza, R.A. Farina, E.M. Malannata, F. Lo Presti, S.A. Balsamo, VOCs photothermo-catalytic removal on MnO_x-ZrO_2 catalysts, Catalysts 12 (1) (2022) 85, https://doi.org/10.3390/catal12010085.

[32] D.P.H. Tran, M.-T. Pham, X.-T. Bui, Y.-F. Wang, S.-J. You, CeO_2 as a photocatalytic material for CO_2 conversion: a review, Sol. Energy 240 (2022) 443–466, https://doi.org/10.1016/j.solener.2022.04.051.

[33] M. Bellardita, R. Fiorenza, L. Palmisano, S. Scirè, Photocatalytic and photothermocatalytic applications of cerium oxide-based materials. in Cerium Oxide (CeO_2): Synthesis, Properties and Applications, Elsevier, 2020, pp. 109–167, https://doi.org/10.1016/B978-0-12-815661-2.00004-9.

[34] X. Guan, S. Jin, L. Liu, X. Zhao, X. Zhang, C. Zhang, Z. Li, C. Fan, Surface engineering of $Ce_xBi_{1-x}O_{2-\delta}$ nanorods rich in oxygen vacancies for enhancing photo-thermal synthesis of dimethyl carbonate from CO_2/CH_3OH, Fuel 358 (2024) 130215, https://doi.org/10.1016/j.fuel.2023.130215.

[35] W.-F. Kuan, C.-H. Chung, M.M. Lin, F.-Y. Tu, Y.-H. Chen, W.-Y. Yu, Activation of carbon dioxide with surface oxygen vacancy of ceria catalyst: an insight from in-situ X-ray absorption near edge structure analysis, Mater. Today Sustain. 23 (2023) 100425, https://doi.org/10.1016/j.mtsust.2023.100425.

[36] M. Lu, D. Jia, H. Xue, J. Tian, T. Jiang, 0D/1D $CuFeO_2$/CuO nanowire heterojunction arrays for improved photoelectrocatalytic reduction of CO_2 to ethanol, J. Alloy. Compd. 960 (2023) 170626, https://doi.org/10.1016/j.jallcom.2023.170626.

[37] J. Liu, J. Yang, Q. Liu, X. Fan, Effect of reduction degree of Ni-phyllosilicate on the catalytic performance for CO_2 methanation: Regulation of catalyst structure and hydroxyl group concentration, Int. J. Hydrog. Energy 48 (2023) 1842–1851, https://doi.org/10.1016/j.ijhydene.2022.10.054.

[38] C. Zhang, H. Yue, Z. Huang, S. Li, G. Wu, X. Ma, J. Gong, Hydrogen production via steam reforming of ethanol on phyllosilicate-derived Ni/SiO_2: enhanced metal–support interaction and catalytic stability, ACS Sustain. Chem. Eng. 1 (2013) 161–173, https://doi.org/10.1021/sc300081q.

[39] E. Hondo, T.Z.H. Gani, M. Kosari, S. Xi, Bella, J. Ashok, J.Y. Tan, T. Wang, H. Bian, K.H. Lim, L. Chen, J. Chang, A. Borgna, S. Kawi, Unveiling the roles of precursor structure and controlled sintering on Ni-phyllosilicate-derived catalysts for low-temperature methane decomposition, ACS Sustain. Chem. Eng. 11 (2023) 8786–8799, https://doi.org/10.1021/acssuschemeng.3c00120.

[40] F. Rao, Y. An, G. Zhu, S. Gong, L. Zhu, H. Lu, X. Shi, Y. Huang, F. Zhang, M. Hojamberdiev, Unveiling the effects of facet-dependent oxygen vacancy on CeO_2 for electron structure and surface intermediates in CO_2 photoreduction reaction, Sep. Purif. Technol. 333 (2024) 125951, https://doi.org/10.1016/j.seppur.2023.125951.

[41] F. Jiang, S. Wang, B. Liu, J. Liu, L. Wang, Y. Xiao, Y. Xu, X. Liu, Insights into the influence of CeO_2 crystal facet on CO_2 hydrogenation to methanol over Pd/CeO_2 catalysts, ACS Catal. 10 (2020) 11493–11509, https://doi.org/10.1021/acscatal.0c03324.

[42] E. Mamontov, T. Egami, R. Brezny, M. Koranne, S. Tyagi, Lattice defects and oxygen storage capacity of Nanocrystalline Ceria and Ceria-Zirconia, J. Phys. Chem. B 104 (2000) 11110–11116, https://doi.org/10.1021/jp0023011.

[43] W.H. Weber, K.C. Hass, J.R. McBride, Raman study of CeO_2: Second-order scattering, lattice dynamics, and particle-size effects, Phys. Rev. B 48 (1993) 178–185, https://doi.org/10.1103/PhysRevB.48.178.

[44] A. Wang, J.J. Freeman, B.L. Jolliff, Understanding the Raman spectral features of phyllosilicates, J. Raman Spectrosc. 46 (2015) 829–845, https://doi.org/10.1002/jrs.4680.

[45] L. Hu, K. Yang, X. Liu, J. Zhu, J. He, X. Chen, Promoted photocatalytic degradation of tetracycline hydrochloride by montmorillonite catalyst loaded with Cu/Mn, J. Mater. Sci. Mater. Electron. 34 (2023) 1471, https://doi.org/10.1007/s10854-023-10862-4.

[46] C. Villanova-de-Benavent, T. Jawhari, J. Roqué-Rosell, S. Galí, J.A. Proenza, Ni-bearing phyllosilicates ("garnierites"): new insights from thermal analysis, μRaman and IR spectroscopy, Appl. Clay Sci. 175 (2019) 47–66, https://doi.org/10.1016/j.clay.2019.03.036.

[47] J. Ashok, Z. Bian, Z. Wang, S. Kawi, Ni-phyllosilicate structure derived Ni–SiO_2 –MgO catalysts for bi-reforming applications: acidity, basicity and thermal stability, Catal. Sci. Technol. 8 (2018) 1730–1742, https://doi.org/10.1039/C7CY02475D.

[48] L. Andrini, R. Moreira Toja, M.R. Gauna, M.S. Conconi, F.G. Requejo, N. M. Rendtorff, Extended and local structural characterization of a natural and 800°C fired Na-montmorillonite–Patagonian bentonite by XRD and Al/Si XANES, Appl. Clay Sci. 137 (2017) 233–240, https://doi.org/10.1016/j.clay.2016.12.030.

[49] P. Anadão, I.L.R. Pajolli, E.A. Hildebrando, H. Wiebeck, Preparation and characterization of carbon/montmorillonite composites and nanocomposites from waste bleaching sodium montmorillonite clay, Adv. Powder Technol. 25 (2014) 926–932, https://doi.org/10.1016/j.apt.2014.01.010.

[50] N. Lahoues-Chakour, S. Barama, A. Barama, B. Djellouli, C. Domingos, A. Davidson, Catalytic behavior of nickel loaded on acid-activated and pillared clay in total gas-phase oxidation of ethanol, J. Nanopart. Res. 20 (2018) 294, https://doi.org/10.1007/s11051-018-4385-1.

[51] M.J. Ahmed, K. Lambrechts, X. Ling, K. Schollbach, H.J.H. Brouwers, Effect of hydroxide, carbonate, and sulphate anions on the β-dicalcium silicate hydration rate, Cem. Concr. Res. 173 (2023) 107302, https://doi.org/10.1016/j.cemconres.2023.107302.

[52] S.A. Balsamo, E. La Greca, M. Calà Pizzapilo, S. Sciré, R. Fiorenza, CeO_2-rGO composites for photocatalytic H_2 evolution by glycerol photoreforming, Materials 16 (2023) 747, https://doi.org/10.3390/ma16020747.

[53] A.A. Atran, F.A. Ibrahim, N.S. Awwad, H.S.M. Abd-Rabboh, M.S. Hamdy, Remarkable enhancement in the photocatalytic activity of porous CeO_2 nanoparticles through nickel doping for wastewater treatment, J. Mater. Sci. Mater. Electron. 34 (2023) 2082, https://doi.org/10.1007/s10854-023-11554-9.

[54] M. Thommes, K. Kaneko, A.V. Neimark, J.P. Olivier, F. Rodriguez-Reinoso, J. Rouquerol, K.S.W. Sing, Physisorption of gases, with special reference to the evaluation of surface area and pore size distribution (IUPAC Technical Report), Pure Appl. Chem. 87 (9-10) (2015) 1051–1069, https://doi.org/10.1515/pac-2014-1117.

[55] Y. Bao, C. Huang, L. Chen, Y. dong Zhang, L. Liang, J. Wen, M. Fu, J. Wu, D. Ye, Highly efficient Cu/anatase TiO_2 {001}-nanosheets catalysts for methanol synthesis from CO_2, J. Energy Chem. 27 (2018) 381–388, https://doi.org/10.1016/j.jechem.2017.12.015.

[56] Z. Qin, X. Wang, L. Dong, T. Su, B. Li, Y. Zhou, Y. Jiang, X. Luo, H. Ji, CO_2 methanation on Co/TiO_2 catalyst: Effects of Y on the support, Chem. Eng. Sci. 210 (2019) 115245, https://doi.org/10.1016/j.ces.2019.115245.

[57] Z. Qin, L. Chen, J. Chen, T. Su, H. Ji, Ni/CeO_2 prepared by improved polyol method for DRM with highly dispersed Ni, Greenh. Gases Sci. Technol. 11 (2021) 1245–1264, https://doi.org/10.1002/ghg.2129.

[58] J.-H. Park, I. Heo, T.-S. Chang, Dry reforming of methane over Ni-substituted $CaZrNiO_x$ catalyst prepared by the homogeneous deposition method, Catal. Commun. 120 (2019) 1–5, https://doi.org/10.1016/j.catcom.2018.11.006.

[59] B. Nematollahi, M. Rezaei, E.N. Lay, Preparation of highly active and stable NiO–CeO_2 nanocatalysts for CO selective methanation, Int. J. Hydrog. Energy 40 (2015) 8539–8547, https://doi.org/10.1016/j.ijhydene.2015.04.127.

[60] M.B. Østergaard, F. Deganello, V. La Parola, L.F. Liotta, V. Boffa, M.K. Jørgensen, Beneficial effect of cerium excess on in situ grown $Sr_{0.86}Ce_{0.14}$ FeO_3 –CeO_2 thermocatalysts for the degradation of bisphenol A, RSC Adv. 13 (2023) 21459–21470, https://doi.org/10.1039/D3RA03404F.

[61] S. Das, J. Ashok, Z. Bian, N. Dewangan, M.H. Wai, Y. Du, A. Borgna, K. Hidajat, S. Kawi, Silica–Ceria sandwiched Ni core–shell catalyst for low temperature dry reforming of biogas: coke resistance and mechanistic insights, Appl. Catal. B Environ. 230 (2018) 220–236, https://doi.org/10.1016/j.apcatb.2018.02.041.

[62] C. Sun, P. Beaunier, V. La Parola, L.F. Liotta, P. Da Costa, Ni/CeO_2 Nanoparticles promoted by Yttrium doping as catalysts for CO_2 methanation, ACS Appl. Nano Mater. 3 (2020) 12355–12368, https://doi.org/10.1021/acsanm.0c02841.

[63] J. Guan, H. Wang, J. Li, C. Ma, P. Huo, Enhanced photocatalytic reduction of CO_2 by fabricating In_2O_3/CeO_2/HATP hybrid multi-junction photocatalyst, J. Taiwan Inst. Chem. Eng. 99 (2019) 93–103, https://doi.org/10.1016/j.jtice.2019.03.007.

[64] X. Zhao, J. Guan, J. Li, X. Li, H. Wang, P. Huo, Y. Yan, CeO_2/3D g-C_3N_4 heterojunction deposited with Pt cocatalyst for enhanced photocatalytic CO_2 reduction, Appl. Surf. Sci. 537 (2021) 147891, https://doi.org/10.1016/j.apsusc.2020.147891.

[65] Y. Li, D. Hui, Y. Sun, Y. Wang, Z. Wu, C. Wang, J. Zhao, Boosting thermo-photocatalytic CO_2 conversion activity by using photosynthesis-inspired electron-proton-transfer mediators, Nat. Commun. 12 (2021) 123, https://doi.org/10.1038/s41467-020-20444-1.

[66] D.R. Mullins, S.H. Overbury, D.R. Huntley, Electron spectroscopy of single crystal and polycrystalline cerium oxide surfaces, Surf. Sci. 409 (1998) 307–319, https://doi.org/10.1016/S0039-6028(98)00257-X.

[67] P. Burroughs, A. Hamnett, A.F. Orchard, G. Thornton, Satellite structure in the X-ray photoelectron spectra of some binary and mixed oxides of lanthanum and cerium, J. Chem. Soc. Dalton Trans. (1976) 1686–1688, https://doi.org/10.1039/dt9760001686.

[68] A. Pfau, K.D. Schierbaum, Pfau Schierbaum, The electronic structure of stoichiometric and reduced CeO_2, surfaces an XPS, UPS and HREELS study, Surf. Sci. 6028 (1994) 71–80, https://doi.org/10.1016/0039-6028(94)90027-2.

[69] G. Pantaleo, V. La Parola, F. Deganello, P. Calatozzo, R. Bal, A.M. Venezia, Synthesis and support composition effects on CH_4 partial oxidation over Ni-CeLa oxides, Appl. Catal. B Environ. 164 (2015) 135–143, https://doi.org/10.1016/j.apcatb.2014.09.011.

[70] Y. Gao, A. Aihemaiti, J. Jiang, Y. Meng, T. Ju, S. Han, X. Chen, J. Liu, Inspection over carbon deposition features of various nickel catalysts during simulated biogas dry reforming, J. Clean. Prod. 260 (2020) 120944, https://doi.org/10.1016/j.jclepro.2020.120944.